The Astrophysical Journal, 612:946–955, 2004 September 10

MILLIMETER AND SUBMILLIMETER SURVEY OF THE R CORONAE AUSTRALIS REGION

Christopher E. Groppi
National Radio Astronomy Observatory, 949 North Cherry Avenue, Tucson, AZ 85721; cgroppi@nrao.edu

Craig Kulesa and Christopher Walker
Steward Observatory, University of Arizona, 933 North Cherry Avenue, Tucson, AZ 85721

and

Christopher L. Martin
Smithsonian Astrophysical Observatory, 60 Garden Street, Cambridge, MA 02138
Received 2004 March 19; accepted 2004 April 24

ABSTRACT

Using a combination of data from the Antarctic Submillimeter Telescope and Remote Observatory (AST/RO), the Arizona Radio Observatory Kitt Peak 12 m telescope, and the Arizona Radio Observatory 10 m Heinrich Hertz Telescope, we have studied the most active part of the R CrA molecular cloud in multiple transitions of carbon monoxide, HCO^+, and 870 μm continuum emission. Since R CrA is nearby (130 pc), we are able to obtain physical spatial resolution as high as 0.01 pc over an area of 0.16 pc^2, with velocity resolution finer than 1 km s^{-1}. Mass estimates of the protostar driving the millimeter-wave emission derived from HCO^+, dust continuum emission, and kinematic techniques point to a young, deeply embedded protostar of $\sim$0.5–0.75 $M_\odot$, with a gaseous envelope of similar mass. A molecular outflow is driven by this source that also contains at least 0.8 $M_\odot$ of molecular gas with $\sim$0.5 $L_\odot$ of mechanical luminosity. HCO^+ lines show the kinematic signature of infall motions, as well as bulk rotation. The source is most likely a Class 0 protostellar object not yet visible at near-IR wavelengths. With the combination of spatial and spectral resolution in our data set, we are able to disentangle the effects of infall, rotation, and outflow toward this young object.

Subject headings: ISM: clouds — ISM: individual (Corona Australis Cloud) — ISM: jets and outflows — ISM: kinematics and dynamics — ISM: molecules — stars: formation

Online material: color figures

1. INTRODUCTION

R Corona Australis (R CrA) is one of the most nearby active star-forming regions, at $\sim$130 pc (Marraco & Rydgren 1981). This close proximity allows for high spatial resolution observations, even with single-dish millimeter-wave and submillimeter-wave telescopes. The cloud is home to many Herbig Ae/Be and T Tauri stars that have been studied extensively in the near-infrared (Wilking et al. 1997). Recent observations in millimeter-wave continuum (Henning et al. 1994) and molecular lines (Harju et al. 1993; Anderson et al. 1997a, 1997b) have shown the existence of active, embedded star formation not directly associated with R CrA, but most likely associated with the Class I source IRS 7 (Taylor & Storey 1984). IRS 7 is the most deeply embedded near-infrared point source in the immediate area.

R CrA was first studied in CO by Loren (1979). His fairly low spatial resolution maps (2.′4) showed large amounts of CO peaking at the general location of R CrA, with high-velocity wing emission throughout the map. The wing emission was later interpreted as a molecular outflow by Levreault (1988). Levreault's higher spectral and spatial resolution data revealed a large bipolar outflow with an extent of over 10′. He also suggested that two outflows might be responsible for the observed morphology and that the embedded source IRS 7 might be responsible for the outflow, not R CrA itself.

In 1985, Wilking et al. used the Kuiper Airborne Observatory to map R CrA in 100 and 50 μm continuum emission (Wilking et al. 1985). The spatial resolution was not adequate to determine if R CrA, IRS 7, or some other unidentified source was driving the continuum and molecular line emission. Since R CrA and IRS 7 are both thought to be high-mass sources visible in the near-IR, there is a possibility that the driving source is neither of these objects. At both 50 and 100 μm, the emission was found to be extended, with a flux density of 570 Jy beam^{-1} at 100 μm. These FIR continuum observations were supplemented by Henning et al. (1994). This 23″ resolution map spatially resolved the region and showed that the peak of the FIR emission is not associated with R CrA, but is much closer to the infrared source IRS 7.

In 1993, Harju et al. performed a large-area (40′ $\times$ 10′) survey of the entire R CrA molecular cloud in $C^{18}O$ (Harju et al. 1993). They estimated that the entire cloud complex contains more than 120 $M_\odot$ of molecular gas. The densest part of this core, centered around IRS 7 and R CrA, contains $\sim$60 $M_\odot$ of molecular gas. Their kinematic analysis showed evidence of rotation around IRS 7 and also clearly identified outflow lobes in the area. Follow-up work by Anderson et al. (1997b) identified a large molecular disk around IRS 7, which shows the kinematic signature of rotation. They mapped the region around R CrA in multiple transitions of HCO^+ to trace the dense gas. In HCO^+, the outflow lobes have an extent of 4′ and show no evidence of the multiple outflows suggested by Levreault. In order to probe the disk dynamics further, the central 2′ $\times$ 2′ region of R CrA was mapped in HCO^+ (3–2). The data show an elongated structure, with three peaks to the northwest, southeast, and south of IRS 7. A slice in centroid velocity through IRS 7 at a position angle of 45° shows signs

of rotation. Anderson et al. then followed up their previous work with HCO^+ (4–3) mapping of the central $2' \times 2'$ around IRS 7, providing improved spatial resolution and kinematic information (Anderson et al. 1997a). The integrated intensity map shows a structure elongated in the north-south direction and unresolved in the east-west direction, peaking on IRS 7. The multilobed structure visible in HCO^+ (3–2) is not present, which they explain as the effect of self-absorption on the line profiles. Velocity centroid maps show a strong velocity gradient near IRS 7, and a slice orthogonal to the gradient at a position angle of about 45° revealed the characteristic signature of rotational motion. They fitted this rotation curve with a disk+central point source model and derived a central mass of 0.8 $M_\odot$. This result points toward the conclusion that the millimeter-wave source is a deeply embedded protostar of fairly low mass.

2. OBSERVATIONS

Observations for this study were performed with the 1.7 m Antarctic Submillimeter Telescope and Remote Observatory (AST/RO), the Steward Observatory Kitt Peak 12 m telescope (KP12m), and the 10 m Heinrich Hertz Telescope (HHT) between 2001 April and 2003 April. We have combined 100 arcmin^2 maps with 0.04–0.06 pc spatial resolution and velocity resolution of less than 1 km s^{-1} in various transitions and isotopes of CO and atomic carbon, with higher resolution mapping of the central region around IRS 7 in CO (3–2) and the high-density molecular tracers HCO^+ (4–3) and $H^{13}CO^+$ (4–3). We have also obtained a fully sampled $10' \times 10'$, 870 μm continuum map of the region at 23″ resolution. These multifrequency, multitransition data give a more complete picture of the active, young, and heavily embedded star formation in the R CrA region. Figure 1 shows spectra in all transitions at the position of IRS 7. The spectra were generated by interpolating all the data cubes to the same number of spatial pixels (25×25) and convolving them to match the 95″ beam size of AST/RO at 460 GHz.

2.1. CO (4–3) *and* [C I] $^3P_1$–$^3P_0$ *Mapping*

CO (4–3) and [C I] $^3P_1$–$^3P_0$ observations were performed at the AST/RO between 2001 November and 2002 January (Stark et al. 2001). For the remainder of this paper we omit the notation for the lower level of the atomic fine-structure transition for brevity. Maps were $10' \times 10'$ (0.4×0.4 pc) in size, fully sampled, and centered on IRS 7. Data were taken with the facility 490/810 GHz receiver, WANDA, in the position-switched mode. Normally, CO (7–6) and [C I] $^3P_2$ are simultaneously observed, along with CO (4–3) or [C I] $^3P_1$, but these data were taken in the austral summer. While weather conditions were adequate for 460 and 490 GHz observations, the atmospheric opacity was too high to effectively observe in the 850 GHz (350 μm) atmospheric window. During observations, system temperatures ranged between 1500 and 9000 K, with typical values of ~4000 K. Facility acousto-optical spectrometers with 1 GHz bandwidth and 1 MHz (0.6 km s^{-1}) resolution were used. Calibration was done with two actively cooled cold loads at 15 and 60 K. Efficiency was measured to be $\eta_{\rm tel} \sim 0.81$, with a beam size of 95″ (0.06 pc; Stark et al. 2001). Data were exported with the facility COMB software tool to individual FITS spectra. These were then compiled into a single CLASS-format data file. The data were then fitted with linear baselines. Processed data cubes were exported in FITS format for further processing with IDL. Typical rms noise for the reduced data cubes is 0.19 and 0.20 K for CO (4–3) and [C I], respectively. Note that isotopic observations of CO were not made. ^{13}CO (4–3), C^{18}O (4–3), and C^{17}O (4–3) all occur at frequencies that are unobservable from the ground, as they are all obscured by pressure-broadened atmospheric water lines.

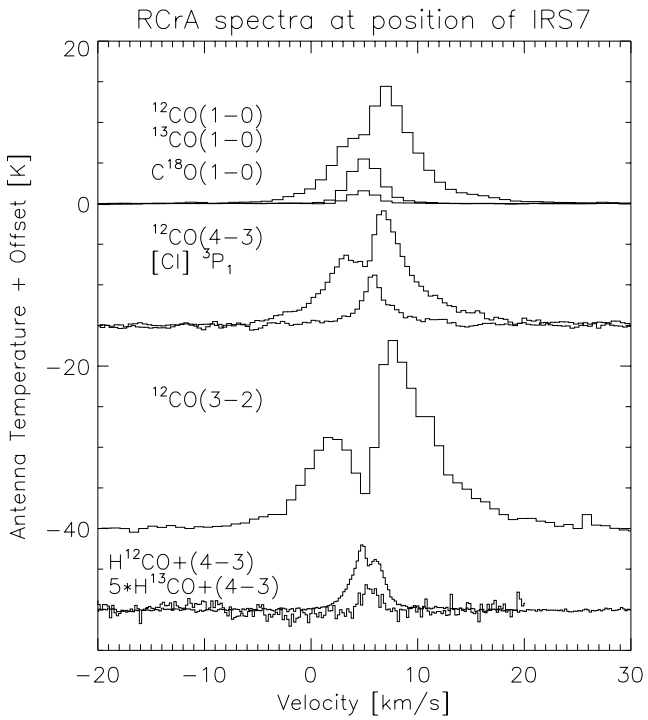

FIG. 1.—Spectra centered on IRS 7 from all our data sources. Spectra were generated by regridding all the maps to the same number of pixels, then convolving the maps to match the largest beam size, 95″. Optically thick CO transitions are dominated by outflow kinematics and are subject to significant self-absorption.

2.2. HCO^+ (4–3) *and* CO (3–2) *Mapping*

In 2001 April we made fully sampled $120'' \times 80''$ (0.07×0.05 pc) maps centered on the embedded infrared source IRS 7 in ^{12}CO (3–2), $H^{12}CO^+$ (4–3), and $H^{13}CO^+$ (4–3) at the HHT. Data were taken in the on-the-fly (OTF) mode with the facility dual-polarization 345 GHz receiver built by the Max-Plank-Institut für Radioastronomie in Bonn, Germany. Typical system temperatures at 15° elevation were $T_{\rm sys} \sim$ 2500 K. The beam size was 23″ (0.01 pc), and the telescope efficiency was $\eta_{\rm tel} \sim 0.7$ (for extended sources). The rms noise for the completed maps was 0.18, 0.14, and 0.14 K, respectively. The respective back ends were 62.5 kHz, 250 kHz, and 1 MHz resolution filter bank spectrometers. The 250 kHz data were used for this work (0.2 km s^{-1}). Calibration was done with an ambient temperature and liquid nitrogen load, using the hot-sky-cold method. Baselines were subtracted using a linear fit, and data were gridded and convolved to a 23″ beam using the GILDAS software package. Data cubes were then exported in the FITS format for further processing using the IDL data processing package.

2.3. ^{12}CO (1–0), ^{13}CO (1–0), *and* C^{18}O (1–0) *Mapping*

CO (1–0) observations were performed at the KP12m in 2003 April. The fully sampled maps are $10' \times 10'$ (0.4×0.4 pc),

centered on IRS 7. Data were taken with the facility 3 mm dual-polarization, single-sideband receiver in OTF mode. The Millimeter Autocorrelator System (MACS) hybrid digital autocorrelation spectrometer was used as the back end, with a 600 MHz bandwidth and 300 kHz (0.8 km s^{-1}) resolution. System temperatures varied between 250 and 1000 K. Several OTF maps per transition were co-added to produce the final data cube. Raw data had linear baseline fits subtracted and were gridded and convolved to a 60″ (0.04 pc) beam size using AIPS software with the standard OTF reduction tools included with the latest AIPS release. Baseline-subtracted and gridded data cubes were then exported via the FITS format for further processing with IDL. Typical rms noise levels are 0.08, 0.01, and 0.03 K for ^{12}CO, ^{13}CO, and C^{18}O, respectively.

2.4. 870 μm *Continuum Mapping*

The 870 μm continuum observations were made at the 10 m HHT in 2003 March. Maps were $10' \times 10'$ (0.4×0.4 pc), centered on IRS 7, and fully sampled. Mapping was done with the facility 19 channel, ^{3}He bolometer array in the OTF mode. Beam size was 23″ (0.01 pc), with a typical efficiency of $\eta_{\rm tel} \sim 0.70$. Data consist of a single OTF map made in less than one hour. Weather was excellent, with the zenith atmospheric opacity measured at 225 GHz of less than 0.05. Opacity at the observation frequency and azimuth was determined via sky dips. Fits to these data show opacity at 343 GHz to be 0.260. Absolute calibration was performed using Mars, assuming a flux at 343 GHz of 741.8 Jy, determined with the GILDAS ASTRO task. Reductions were performed using the GILDAS NIC package. Scans were despiked, gridded, and restored using standard NIC tools. Reduced and calibrated maps were exported via the FITS format for further processing with IDL. The rms noise in the map is 0.3 Jy beam^{-1}, assuming the worst-case noise at the edge of the map.

3. ANALYSIS

3.1. *Morphology*

Our survey concentrates on a $10' \times 10'$ field centered around IRS 7. This encompasses the peak of the submillimeter continuum emission near IRS 7 and is a local maximum for the molecular gas emission. Since optical depth effects severely effect the morphology of the ^{12}CO measurements, we use our 870 μm continuum map, along with the optically thin tracers of ^{13}CO (1–0) and C^{18}O (1–0), to trace the dust and gas mass in the region. Both the gas and the dust show the same qualitative morphology, peaking around IRS 7, with extended emission toward the northwest. The continuum emission is very strongly peaked around IRS 7, with extended emission at flux levels $\sim$10 times lower than the peak. Emission in optically thin CO isotopes peaks at the same location but is much more extended, with a second peak $\sim$200″ to the northwest. Emission above the 3 σ detection limit extends throughout most of the mapped region but is generally oriented from the southeast to the northwest. Features in the CO emission do not tend to correlate with the positions of the brightest infrared point sources in the region. A map of the central $120'' \times 80''$ in the high-density tracer HCO$^+$ (4–3) at 23″ spatial resolution reveals the "molecular disk" detected by Anderson et al. (1997b). The high-density gas traces a structure elongated in declination relative to right ascension with an aspect ratio of about 3 : 1. The continuum data, with the same spatial resolution, also clearly show this elongated structure in the central region of the map. A hint of the structure is also seen in the CO maps, but the larger 60″ beam size of these data masks the disk. Maps of these data are presented in Figure 2.

3.2. *FIR Spectral Energy Distribution*

We have combined our measured peak flux for the 870 μm emission with 1.3 mm data from Henning et al. (1994) and *IRAS* 100, 60, 25, and 12 μm fluxes from the *IRAS* Point Source Catalog to produce an FIR spectral energy distribution (SED) of the R CrA core. The 1.3 mm and 870 μm measurements were done via OTF mapping, with virtually identical beam sizes. The *IRAS* beam is much larger ($\sim$100″), but the millimeter and submillimeter emission is strongly peaked at the central position. This large beam could cause significant contamination of these frequency points. We consider only the 100 and 60 μm fluxes when fitting a single diluted blackbody to the SED, since the two shorter wavelength bands are likely to contain contributions from hot dust. The SED shape bears this out. Since we are only concerned with the cold dust associated with the millimeter and submillimeter line emission, we do not attempt to fit a hotter second blackbody component. We fit the FIR SED with a diluted blackbody SED, varying the parameters of source size, temperature, and spectral index (Walker et al. 1990a). Figure 3 shows the SED with our fit to the four lowest frequency points. We determine the fit parameters to be $\Omega_s = 3.05 \times 10^{-9}$ sr, $T = 36.4$ K, and $\beta = 1.66$. Formal errors in the fit are insignificant compared to the uncertainties involved in the simple model for the SED and the later estimates of dust and gas masses. The temperature and spectral index are comparable to those of other dust cores (Walker et al. 1990a), but the beam filling factor is rather large at 0.31. This is explained by the close proximity of R CrA, only 130 pc. We then measure the FIR luminosity by integrating under the fit and determine the luminosity to be 21.1 $L_\odot$, typical for a low-mass, young protostar. We can also use these data to estimate the dust and gas mass in the core, if the dust is optically thin. The dust opacity at 870 μm is 0.016, allowing us to follow Hildebrand to estimate the dust mass (Hildebrand 1983):

$$M_d = \frac{F_\nu D^2}{Q_\nu B_\nu(T)} \frac{4a\rho}{3}, \tag{1}$$

where

$$Q_\nu = 7.5 \times 10^{-4} \left(\frac{125\ \mu\text{m}}{\lambda} \right)^\beta \tag{2}$$

and a and ρ are the grain radius and density, respectively. We assume 0.1 μm for a and 3 g cm^{-2} for the grain density. Assuming a gas-to-dust ratio f of 100, we can estimate the molecular hydrogen mass and column density. We calculate an H_2 mass of 0.6 $M_\odot$ and an H_2 column density of 7.3×10^{23} cm^{-2} for the central 23″ region centered on the peak of the FIR emission. The results using the dust opacities of Draine & Lee (1984) are lower by about 30%. These estimates are accurate only to within a factor of several, because of the uncertainties introduced by the large *IRAS* beam, but are consistent with the parameters determined through other methods.

3.3. *Core Mass and Kinematics via* HCO$^+$(4–3)

Using the higher spatial resolution (23″) $120'' \times 80''$ H^{12}CO$^+$ (4–3) and H^{13}CO$^+$ (4–3) maps of the IRS 7 region,

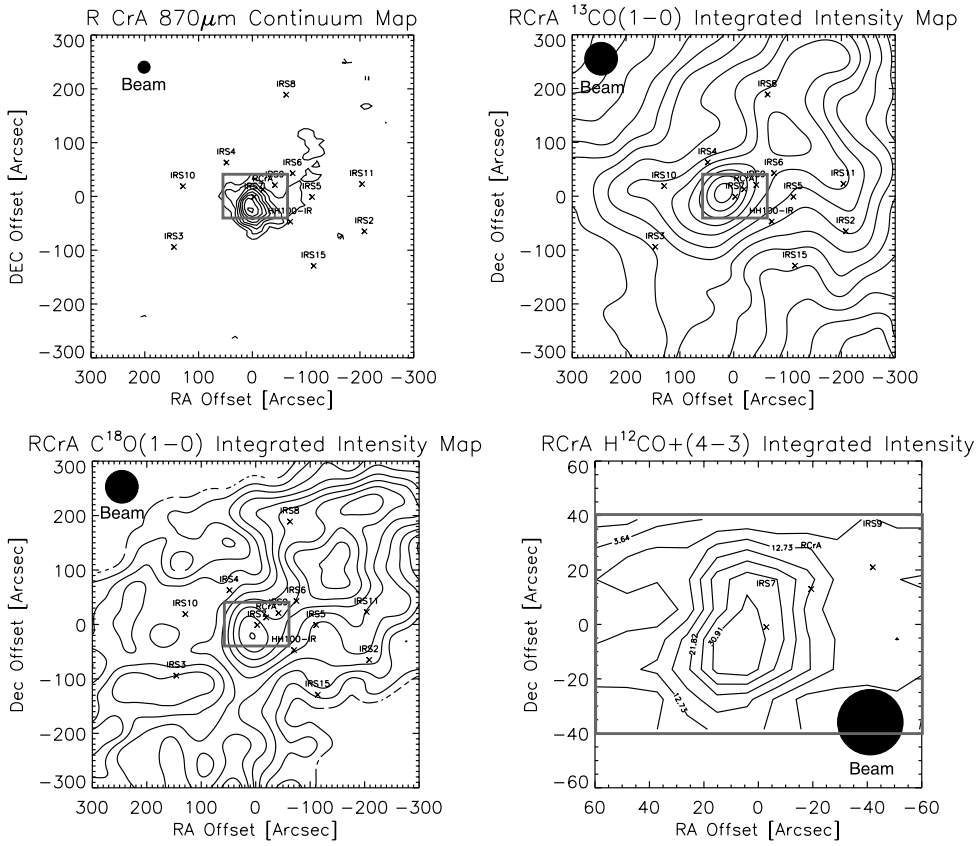

FIG. 2.—Maps ($10' \times 10'$) in 870 μm continuum emission, ^{13}CO integrated intensity, and C^{18}O integrated intensity and an $80'' \times 120''$ map in HCO$^+$ (4–3) integrated intensity. Minimum contours are at the 2 σ level, with 2 σ contour spacing. Beam sizes are specified in each map. The continuum emission from cold dust is well traced by the optically thin CO emission. The HCO$^+$ inset shows the "molecular disk" structure reported by Anderson et al. (1997a), elongated along the north-south axis. [*See the electronic edition of the Journal for a color version of this figure.*]

we have determined the central mass of the FIR emission peak through LTE estimates of the gas column density and through the kinematic signature of the rotation of the molecular disk. Anderson et al. determined the central mass, using HCO$^+$ (4–3) observations, via the kinematic method. This gives four independent measures of the central mass of the dust core, giving us some confidence in determining the properties of the central source (Anderson et al. 1997a).

With both H^{12}CO$^+$ and H^{13}CO$^+$ measurements at the central position, we can estimate the column density of HCO$^+$ and then estimate a column density of H_2, assuming an abundance for HCO$^+$. For simplicity, we assume that the gas is in LTE. The line shape of H^{12}CO$^+$ clearly shows the effects of self-absorption, so the LTE formalism will overestimate optical depth and therefore overestimate the column density and mass. The effects of self-absorption on the optically thick line's integrated intensity are unlikely to be more than a factor of 2, overestimating the mass by a factor of a few. More complicated microturbulent methods can be used to take the effects of self-absorption into account, but many more assumptions are necessary. We calculate the optical depth from the ratio of the optically thick to optically thin species:

$$\frac{I_{\rm thick}}{I_{\rm thin}} = \frac{1 - e^{-r_a \tau}}{1 - e^{-\tau}}, \qquad (3)$$

where $I_{\rm thick}$ and $I_{\rm thin}$ are the integrated intensities of the optically thick and thin species, respectively, r_a is the abundance ratio of the optically thick to the optically thin species, and τ is the optical depth of the optically thin species. For our analysis, we assume an H^{12}CO$^+$–to–H^{13}CO$^+$ abundance ratio of 60 and that the gas excitation temperature is given by the peak H^{12}CO$^+$ line temperature divided by the telescope efficiency ($\sim$0.7). This most likely underestimates the excitation

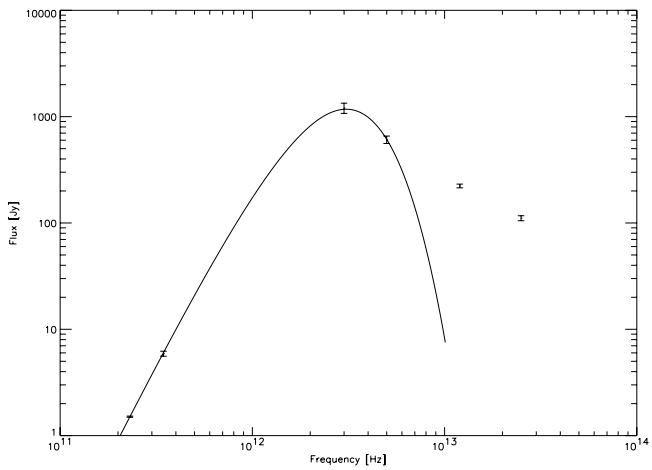

FIG. 3.—FIR SED of the R CrA region centered on IRS 7. The 870 μm point is from this work. The 1300 μm point is from Henning et al. (1994) data taken with the 19 channel facility bolometer array at SEST. The FIR data are *IRAS* measurements of R CrA. Since the *IRAS* beam is $\sim$100$''$, some contamination from the surrounding material off the dust emission peaks is present. We fit only the 100 and 60 μm points, to exclude contributions from hot dust. Error bars are ± 1 σ.

temperature, which partially counters the effect of the overestimate in optical depth. From the optical depth and excitation temperature, we can then calculate the column density of the optically thin species $N_{\nu,\mathrm{thin}}$:

$$N_{\nu,\mathrm{thin}} = T_{\mathrm{ex}}\tau\Delta\nu\frac{6k}{8\pi^3\nu\mu^2}\left(\frac{2l+1}{2u-1}\right)\left(\frac{e^{[(l/2)/(h\nu/kT_{\mathrm{ex}})]}}{1-e^{-(h\nu/kT_{\mathrm{ex}})}}\right), \quad (4)$$

where l is the lower rotational level, u is the upper rotational level, μ is the dipole moment of the molecule, and $\Delta\nu$ is the frequency interval over which the integrated intensity is measured. At the peak of the map, we calculate an excitation temperature of 15 K, an optical depth for $H^{13}CO^+$ of 0.04, and an H_2 column density of 2.2×10^{23} cm^{-2}. This translates to a gas mass in the central beam of 0.5 $M_\odot$, for an abundance ratio of $H^{12}CO^+$ to H_2 of 10^{-9} (Hogerheijde 2002).

We can also estimate core mass through gas kinematics from velocity centroid maps. We calculate the velocity centroid of each map position, following Adelson & Leung (1982):

$$v_c = \frac{\sum_i (V_{\mathrm{Dopp}})_i (T_A)_i}{\sum_i (T_A)_i}, \quad (5)$$

where V_{Dopp} is the velocity offset from line center and T_A is the line brightness at the offset velocity, indexed by velocity channel i. The result is a map of line centroid velocity, where the line centroid is the velocity at which the integrated intensity redward and blueward of the centroid velocity is the same. This gives a measure of the kinematics of the object averaged over the line. We compute the centroid velocity over the range -3.0 to $+2.5$ km s^{-1}, which encompasses the entire line core at the central position and averages over self-absorption effects. The resulting map is shown in Figure 4. We take a slice at a position angle of 120°, orthogonal to the velocity gradient. The map has been interpolated by a factor of 3 in both dimensions. A slice centered on IRS 7 was averaged over three columns to produce the rotation curve. We then assume circular motion around a point mass to determine an upper limit for the central mass:

$$M_c = \frac{v^2 r}{G}, \quad (6)$$

where we define v as the half-amplitude of the rotation curve and r as half the distance between peaks in the curve. We determine a rotational velocity of 0.47 ± 0.04 km s^{-1}, a radius of 0.015 ± 0.001 pc, and a derived mass of 0.75 ± 0.15 $M_\odot$, assuming a 3″ pointing error and errors in the velocity centroid according to Narayanan et al. (1998). This is consistent with the Anderson et al. (1997a) result of 0.8 $M_\odot$.

3.4. *Outflow*

In the convolved spectra of Figure 1, it is clear that the optically thick species show extended wing emission at high velocities. We made outflow maps by calculating the integrated intensity in the line wings for ^{12}CO (1–0), ^{13}CO (1–0), ^{12}CO (4–3), and [C I] $^3P_1$. We use the convolved spectra to determine the velocity range of the wing material. Figure 5 shows the resulting outflow maps and the location of known infrared sources in the area. Optical depth effects alter the morphology of the ^{12}CO maps, as compared to the ^{13}CO map. In [C I], only the red outflow lobe is clearly visible.

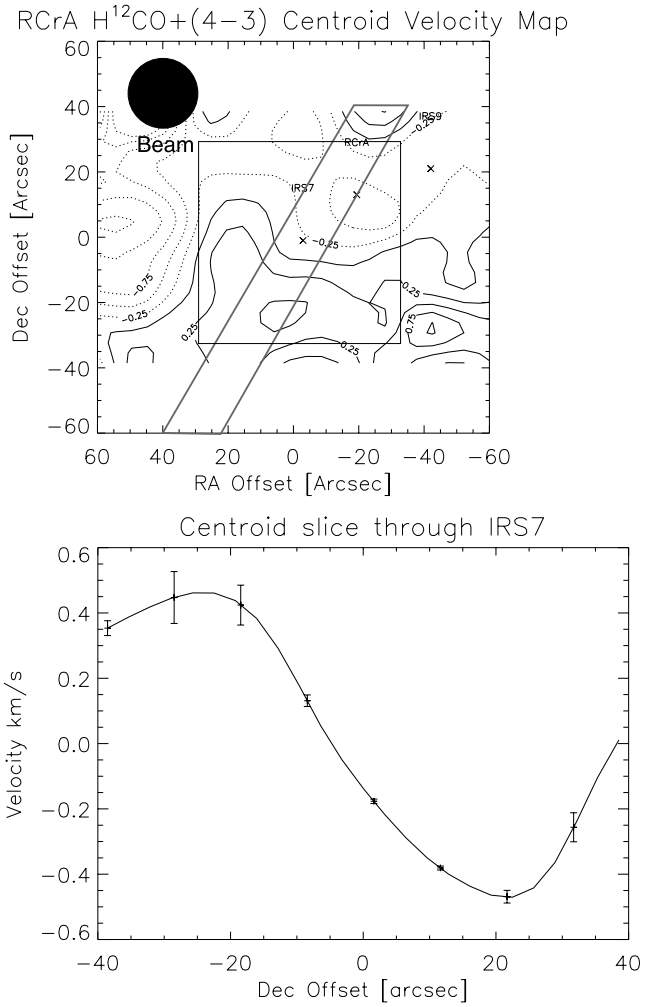

FIG. 4.—*Top*: HCO^+ (4–3) centroid velocity plot. Contours are 0.25 km s^{-1}, with dotted contours denoting negative velocity. *Bottom*: Slice denoted by the box in the top plot, showing the signature of rotation. The centroid velocity plot also shows evidence of the "blue bulge," a sign of infall motion. [*See the electronic edition of the Journal for a color version of this figure.*]

Over the velocity ranges -4 to 3 and 8–15 km s^{-1}, we can use both ^{12}CO (1–0) and ^{13}CO (1–0) outflow data to compute the column density of CO. The peak antenna temperatures for CO (1–0), CO (3–2), and CO (4–3) are all similar (see Fig. 1), suggesting that the gas is thermalized. We assume that the peak line temperature, corrected for efficiency, is the excitation temperature in the outflow. In addition, the ratio of CO to H_2, while not exactly known, is expected to vary less across the galaxy than the HCO^+/H_2 abundance ratio (Hogerheijde 2002). As is clear from the ^{12}CO (1–0) spectrum at the center position, the optical depth in the blue wing is much higher than that in the red, because of either foreground obscuration or self-absorption. We find blue wing and red wing masses of 0.46 and 0.38 $M_\odot$, respectively, assuming an abundance ratio of ^{12}CO to ^{13}CO of 60 and a ^{13}CO/H_2 abundance ratio of 2.5×10^{-6}. The characteristic age of the outflow is found by dividing the extent of the outflow by the maximum observed velocity from line center, v_c. We take 300″ as the outflow extent and 17 km s^{-1} as the maximum velocity, which gives a characteristic age of 10^4 yr. Using these values, we can calculate the characteristic values for the momentum, Mv_c,

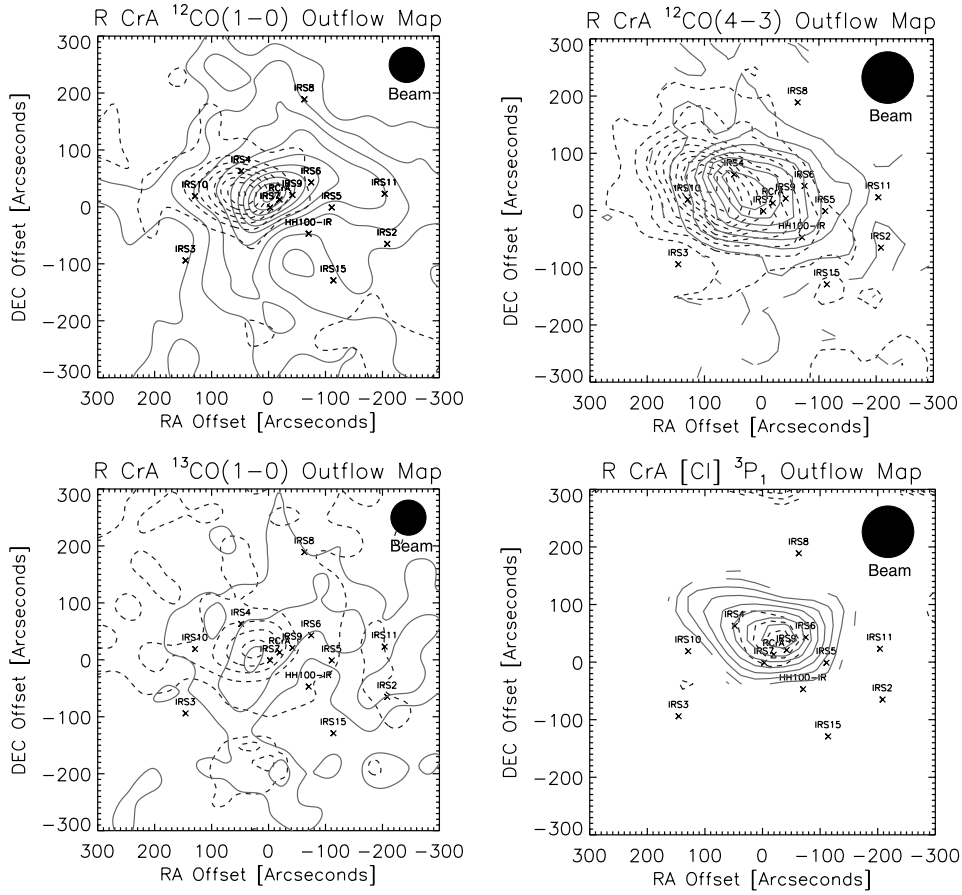

FIG. 5.—Outflow maps of R CrA. Panels are for ^{12}CO (1–0), ^{12}CO (4–3), ^{13}CO (1–0), and [C I] $^3P_1$. Minimum contours are 2 σ, with 2 σ contour spacing. The ^{12}CO (1–0) and ^{12}CO (4–3) blue wing velocity interval is −10 to 3 km s^{-1}, while the red interval is 8–22 km s^{-1}. The ^{13}CO (1–0) and [C I] blue wing interval is −4 to 3 km s^{-1}, while the red wing interval is 8–15 km s^{-1}. Dashed contours denote negative velocities. [*See the electronic edition of the Journal for a color version of this figure.*]

the kinetic energy, $\frac{1}{2}Mv_c^2$, the outflow mechanical luminosity, $KE/$age, and the mass outflow rate, $M/$age. Outflow mass and energetics are summarized in Table 1.

None of the isotopic forms of CO (4–3) are observable from the ground because of atmospheric absorption due to water and molecular oxygen. For this transition, the outflow mass and energetics are determined by assuming that the line wing emission is optically thin. This assumption provides a lower limit to the outflow mass. We again assume that the excitation temperature is the peak CO line temperature divided by the telescope efficiency, 0.81 for AST/RO at 460 GHz (Stark et al. 2001). We follow Snell et al. (1984) to determine the column density of ^{12}CO, assuming that the emission is optically thin:

$$N_{\rm CO} = \frac{4.2 \times 10^{13} T_{\rm ex} \int T_R({\rm CO})\, dV}{\exp(-h\nu/E)}\ {\rm cm}^{-2}. \qquad (7)$$

The derived outflow masses (0.40 and 0.32 $M_\odot$) are similar to those determined from CO (1–0). This is not surprising if the gas in the region is relatively warm. We can also apply the same approach to the ^{12}CO (1–0) data to see the effects of taking optical depth into account. Masses are calculated to be 0.21 and 0.06 $M_\odot$ for the red and blue wings, respectively.

TABLE 1
R CrA OUTFLOW ENERGETICS

Line Wing and Method	Mass ($M_\odot$)	Momentum (g cm s^{-1})	Kinetic Energy (g cm^2 s^{-2})	Mechanical Luminosity ($L_\odot$)	Mass Outflow Rate ($M_\odot$ yr^{-1})
CO (1–0) LTE red	0.38	1.3×10^{39}	1.1×10^{45}	0.44	3.6×10^{-5}
CO (1–0) LTE blue	0.46	1.6×10^{39}	1.3×10^{45}	0.53	4.3×10^{-5}
^{12}CO (1–0) optically thin red	0.21	7.2×10^{38}	6.1×10^{44}	0.25	2.0×10^{-5}
^{12}CO (1–0) optically thin blue	0.06	2.2×10^{38}	1.9×10^{44}	0.07	6.0×10^{-6}
^{12}CO (4–3) optically thin red	0.40	1.4×10^{39}	1.2×10^{45}	0.46	3.8×10^{-5}
^{12}CO (4–3) optically thin blue	0.32	1.1×10^{39}	9.3×10^{44}	0.37	3.1×10^{-5}

The value for the red wing is within a factor of 2 of the value obtained by the LTE analysis, but the blue wing mass is several times lower. This is due to the higher optical depth in the blue wing of the ^{12}CO (1–0) lines.

4. DISCUSSION

4.1. *A Possible Class 0 Source Driving the FIR Emission*

In most previous research, it is assumed that the molecular line and FIR emission in the region is directly associated with R CrA. However, work by Harju and Anderson suggested the embedded Class I source IRS 7 as the most likely driving source for this emission (Harju et al. 1993; Anderson et al. 1997a, 1997b). The possibility exists that the peak of the millimeter-wave and submillimeter-wave emission, and the driving source for the molecular outflow(s) in the region, might be not IRS 7 but a more deeply embedded source not detected in infrared surveys to date. The results presented here suggest that the source of the molecular line and cold dust emission may be a deeply embedded Class 0 source within $\sim$10″ of IRS 7, with a mass of about 0.5 $M_\odot$.

Recent work by Chini et al. (2003) concludes that IRS 7 is not the driving source behind the millimeter-wave emission in the region. Their 1.3 mm continuum map of the region identifies 25 dust emission peaks. The peak near IRS 7, called MMS 13, is coincident with neither the thermal IR source associated with IRS 7 from Wilking et al. (1997) nor the VLA sources from Brown (1987), but is located $\sim$15″ south. They conclude that MMS 13 is most likely a deeply embedded Class 0 source, although their continuum flux suggests a source mass of 5 $M_\odot$ for 20 K dust. Our data also seem to suggest that the driving source is south of IRS 7, but our spatial resolution is not adequate to make a firm determination. Recently, 50 GHz continuum interferometric imaging of the region was performed by Choi & Tatematsu (2004). They find an elongated structure with a position angle of $\sim$120°, located $\sim$5″ to the north of IRS 7. The elongated structure has an SED consistent with dust emission, while the emission peak at the position of IRS 7 has an SED suggesting free-free or nonthermal emission. Millimeter-wave interferometric observations toward IRS 7 in one or more molecular lines (e.g., CO, HCO^+, and CS) are needed to identify the location of the driving source.

Other evidence exists that suggests the source of the emission to be a Class 0 object. The mass of the molecular core can be estimated three ways: (1) a kinematic measure (Fig. 4) of the total mass of the protostar and surrounding gas, (2) the FIR continuum flux, and (3) the column density of HCO^+. All three of these measurements have considerable uncertainty, but taken together they point toward a deeply embedded source of about 0.5 $M_\odot$ with a gaseous envelope of a similar mass.

The kinematic measurement from the centroid velocity of HCO^+ (4–3) shows a velocity gradient strongly suggestive of rotation. If this velocity gradient is due to rotation, then a lower limit to the enclosed mass can be derived. In the 0.030 pc diameter volume about the center of motion, we derive a gravitational mass of 0.75 $M_\odot$. This assumes that all the mass is concentrated at the center.

We also estimate the gas mass in the central 22″ (about half the distance between velocity peaks in the velocity gradient) via continuum observations. Assuming that the dust emission arises from 0.1 μm radius silicate dust grains with a dust emissivity $\propto\lambda^{-2}$ and that the dust-to-gas ratio is $\sim$100, we compute a total gas mass for the core of 0.6 $M_\odot$. This determination has considerable uncertainty because of the use of *IRAS* data in the determination of the SED, but it is consistent with the masses derived using other methods.

The measurement of the H_2 mass via HCO^+ also gives a similar answer. We use $H^{12}CO^+$ and $H^{13}CO^+$ measurements with a 22″ beam size to estimate the column density of H_2. Both the varying abundance of HCO^+ relative to H_2 and the effects of self-absorption are uncertain. The presence of self-absorption will lead to overestimates of the HCO^+ column density. Assuming an HCO^+/H_2 abundance ratio of 10^{-9} and neglecting the effects of self-absorption, we estimate a gas mass of 0.5 $M_\odot$. While uncertain, both these measurements point to a total envelope mass on the order of the mass of the central source. In addition, the somewhat small FIR luminosity of 21 $L_\odot$ is similar to that of low-mass protostars of about 0.5 $M_\odot$ (Walker et al. 1990b). We suggest that the driving source for the outflow is a previously unidentified Class 0 protostar located $\sim$10″ from IRS 7 at the peak of the millimeter-wave continuum emission, referred to by Chini et al. (2003) as MMS 13.

4.2. *Infall*

Spectral lines of Class 0 protostellar objects sometimes show the classic spectral signature of infall (Walker et al. 1986). As seen in Figure 6, HCO^+ (4–3) spectra near the center position of the map show an enhanced blue peak, characteristic of this infall signature. In addition, the centroid velocity map in Figure 4 shows the "blue bulge" signature of infall motion (Walker et al. 1994). North and south of the central position, rotation begins to dominate the kinematics. At about 30″ east and west of the source, the outflow dominates the appearance of the line profiles in the HCO^+ map. In CO maps, the outflow completely masks all signs of rotation and infall. Only in dense gas tracers (e.g., HCO^+) do all the intertwined motions reveal themselves near the source. Convolving spectra to larger beam sizes, we continue to see a line shape suggestive of infall. In Figure 7, the HCO^+ spectrum has been convolved in half-beam increments from 22″ to 77″, which is essentially the entire HCO^+ (4–3) map. The infall line shape is still clearly visible in all the spectra, suggesting that infall is occurring over the entire central region around the protostellar source. This points toward an infall region of at least 6000 AU in radius. Using our measurements of FIR luminosity and temperature, we can estimate the mass infall rate for this object. If all the FIR luminosity is generated through accretion, then

$$L_{\rm FIR} = \frac{GM\dot{M}}{r}, \tag{8}$$

where r is the radius of the protostar and M is the mass of the protostar. We assume 2×10^{11} cm for the radius, about 3 $R_\odot$ (Stahler et al. 1980), and 0.5 $M_\odot$ for the mass of the central object, given our mass estimates of the source+envelope and envelope masses. This leads to a mass accretion rate of 4×10^{-6} $M_\odot$ yr^{-1}, uncertain to within a factor of a few. A mass infall rate can also be computed for the case of self-similar collapse. Assuming a sound speed due to only thermal pressure, and ignoring magnetic and turbulent support, the mass accretion rate is given by (Shu 1977)

$$\dot{M} = \frac{0.975a^3}{G}, \tag{9}$$

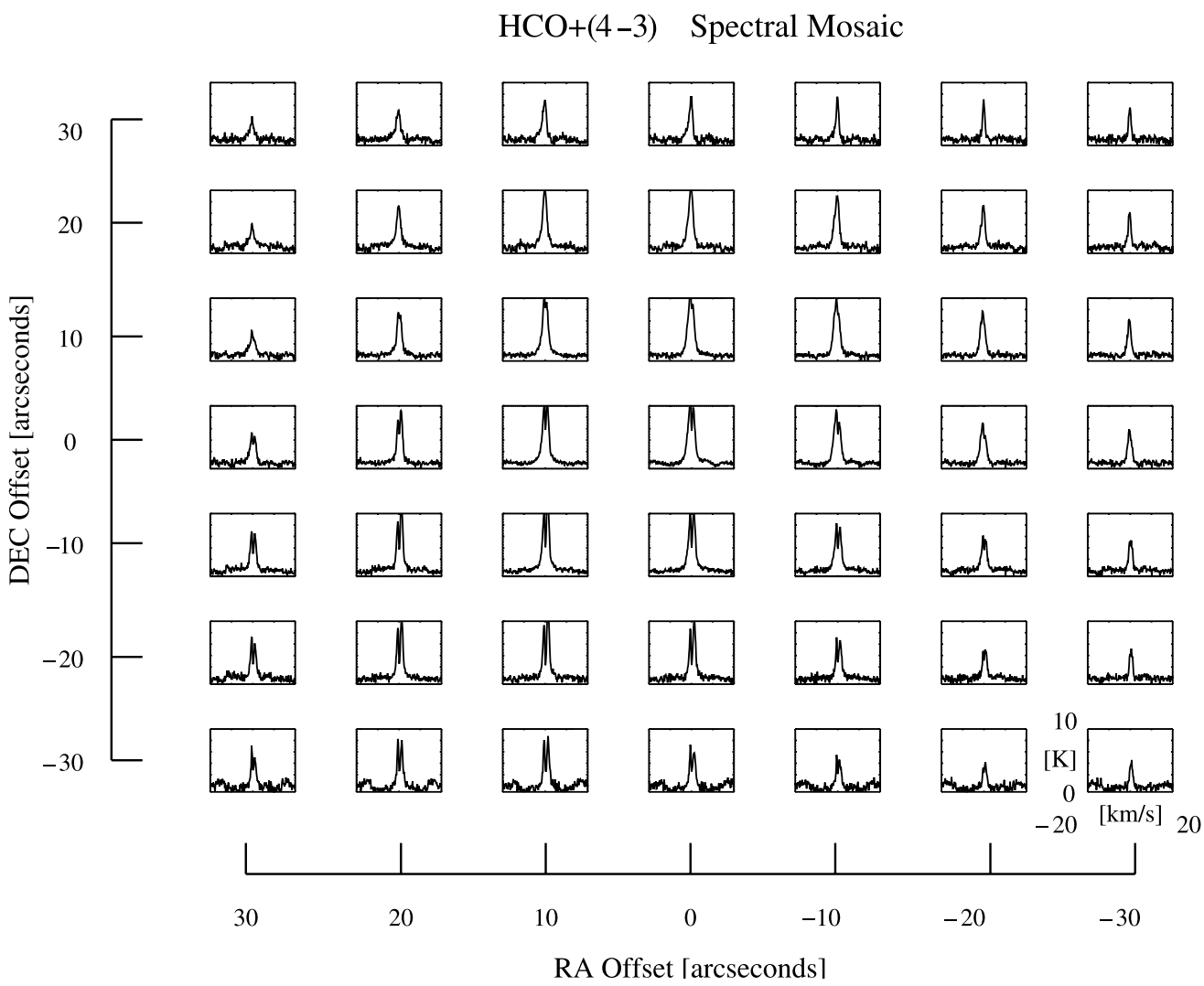

FIG. 6.—$H^{12}CO^+$ (4–3) spectral line mosaic of a $60'' \times 60''$ region centered on IRS 7. The y-axis of each spectrum is T_A^* (in kelvins) and the x-axis is velocity (in km s^{-1}). The box in Fig. 2 marks the location of the mosaic.

where

$$a = \sqrt{\frac{kT}{m_{H_2}}}. \tag{10}$$

Substituting the gas temperature derived from the observed SED (~36 K), we find a mass accretion rate of $1 \times 10^{-5}\ M_\odot\ yr^{-1}$. Both these estimates are consistent with a low-mass, Class 0 source.

4.3. *Atomic Carbon Distribution*

In the canonical picture of carbon in a molecular cloud, an "onion-skin" model is used, in which the carbon is ionized in the outer layer of the cloud as [C II]. Further in the cloud, where the carbon is more shielded, it is in atomic form as [C I]. Deeper in the cloud, the carbon forms CO. In some cases, where the cloud material is very clumpy, this same picture holds, but now each clump acts as a small cloud, causing [C II] and [C I] to appear well mixed throughout the cloud (Stutzki et al. 1988). We see evidence of both these effects in our carbon observations. To reveal enhancement of [C I] relative to $C^{18}O$, we calculated the column density of both species, assuming that they are both optically thin. We estimated the column density of the atomic carbon, following Walker et al. (1993):

$$N_C = \frac{N_1}{3}\left(e^{23.6/T_{ex}} + 3 + 5e^{-38.8/T_{ex}}\right), \tag{11}$$

where

$$N_1 = 5.94 \times 10^{15} \int v T_{mb}\, dV\ \text{cm}^{-2}. \tag{12}$$

We then plotted the ratio of [C I]/$C^{18}O$ column density normalized to the average over the map to look for enhancement/depletion of atomic carbon relative to CO, considering only locations where both the [C I] and the CO integrated intensities were larger than the 2 σ noise level. The results are shown in Figure 8. As expected from the canonical picture, [C I] is enhanced at the edges of the cloud and depleted toward the center. We have plotted the contours over an optical image of the region from the Palomar Sky Survey. The regions of low relative [C I] abundance correlate with the regions of high optical extinction and the region with strong FIR continuum emission.

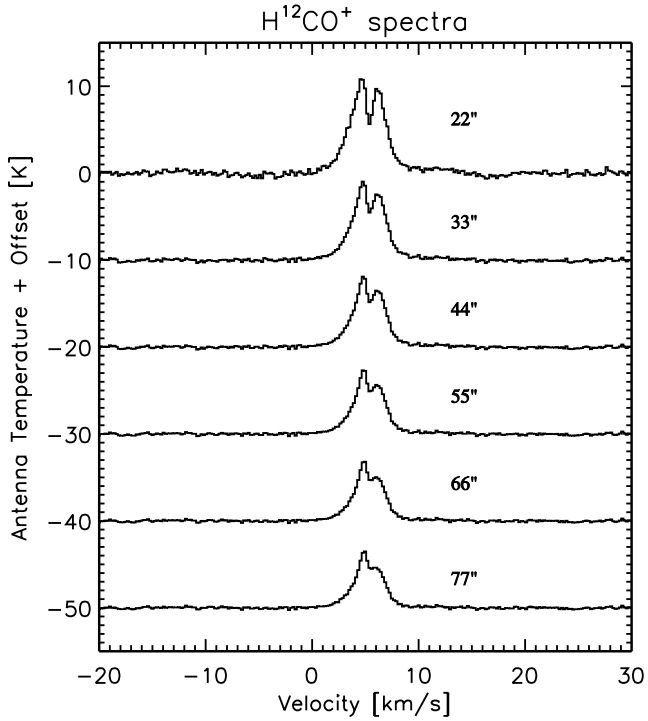

FIG. 7.—HCO^+ (4–3) spectra, centered on IRS 7. Spectra were produced from an OTF map, convolved in half-beam increments from 22″ to 77″.

In the outflow map of Figure 5, we see that carbon is observed throughout the red wing of the outflow. Only a small amount of carbon is visible in the blue wing. While the [C I] is not as ubiquitous as ^{13}CO in the outflow, it is still visible, and it does not appear to be in a shell configuration. This leads us to believe that while atomic carbon is enhanced at the edge of the cloud, some atomic carbon is still mixed throughout the cloud, pointing to clumpy structure even in the outflow.

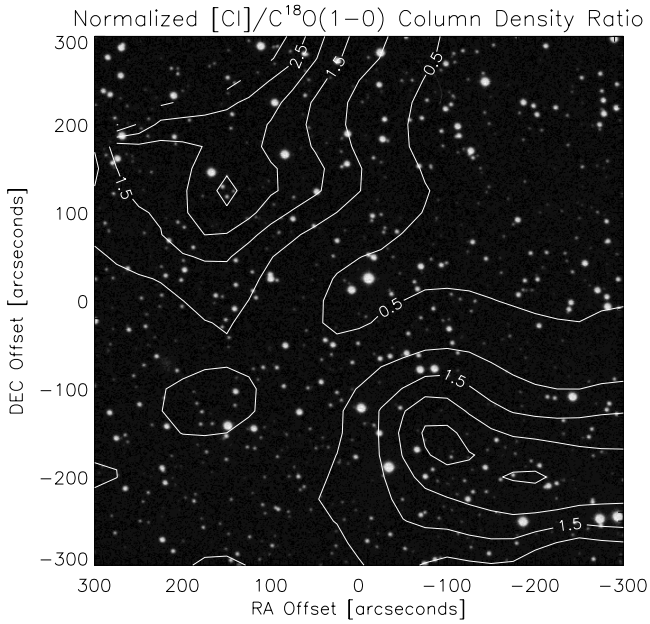

FIG. 8.—Normalized [C I] $^3P_1$–to–$C^{18}O$ (1–0) column density ratio. Contours are overlaid on a Palomar Sky Survey image of the region. In areas of high visual extinction, the abundance of [C I] drops relative to CO, as expected, with an increased [C I]/CO ratio at the edges of the regions of high visual extinction.

4.4. *System Configuration*

The kinematic signs of rotation, infall, and outflow, combined with the distribution of CO, HCO^+, and submillimeter continuum emission, all combine to produce a picture of star formation in the R CrA molecular core. Because of the proximity of R CrA, the kinematic signatures of infall, rotation, and outflow can be tentatively identified and disentangled. A proposed configuration for the MMS 13 core is shown in Figure 9, overlaid on the centroid velocity plot of HCO^+ (4–3). We believe that a highly embedded Class 0 protostellar source is the driver for the FIR emission in the area. Kinematic and morphological evidence point to a location within $\sim 10''$ of the Class I source IRS 7. This source, located at the peak of the millimeter-wave continuum emission, was tentatively identified by Chini et al. (2003) as MMS 13. This source is surrounded by a rotating molecular disk, first observed by Anderson et al. (1997a, 1997b). Our HCO^+ (4–3) measurements point to a similar conclusion, with an enclosed mass of $0.75 \pm 0.15\ M_\odot$. Mass estimates based on derived gas column density, 870 μm continuum measurements, and dynamical arguments suggest a central protostar of $\sim 0.5\ M_\odot$, with an envelope of similar mass. We postulate that the disk major axis is at a position angle of about 60°. This position angle gives the cleanest rotational signature in the velocity gradient and is consistent with the emission and the orientation of the molecular outflow. This molecular disk has a major axis of $\sim$2500 AU and is unresolved in the orthogonal direction in all our observations. In the central 20″–30″ of the HCO^+ (4–3) map, the line profiles show a strong infall line shape. This shape persists when the spectra are convolved to

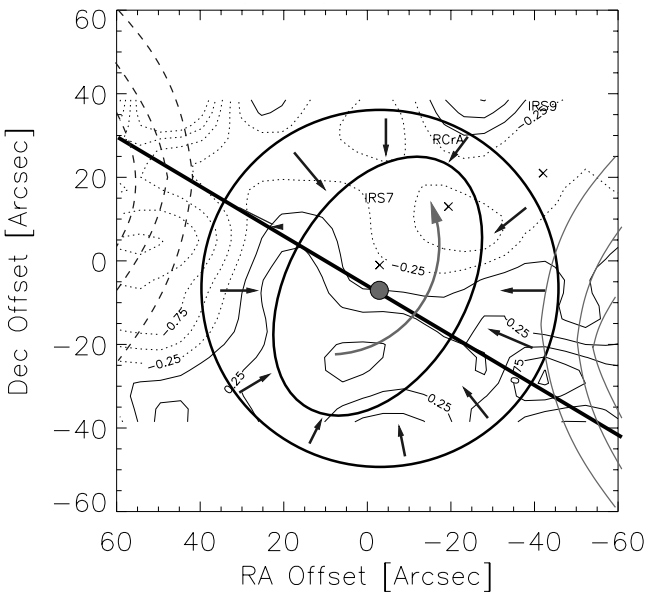

FIG. 9.—Schematic of our proposed system configuration. The contours show the combined effects of rotation, infall, and outflow. The morphology suggests the existence of a Class 0 source within $\sim 10''$ of IRS 7, surrounded by a $\sim$2500 AU radius molecular disk at a position angle of 60°. The envelope surrounding this disk exhibits signs of infall. Toward the east and west edges of the map, outflow kinematics begin to dominate. The diagram is overlaid on the HCO^+ (4–3) centroid velocity plot. [*See the electronic edition of the Journal for a color version of this figure.*]

beam sizes as large as the entire HCO^+ map. In addition, the central region of the centroid velocity plot shows the blue bulge signature of infall motion. This infall region is at least 6000 AU in radius, surrounding the molecular disk. At distances larger than 6000 AU, the kinematics of the molecular outflow begin to dominate the line profiles. At lower spatial resolution, and with more sensitivity to the lower density gas, CO maps are virtually all dominated by the outflow and the ambient cloud material.

5. SUMMARY

We have observed the molecular core near R CrA in ^{12}CO (1–0), ^{13}CO (1–0), $C^{18}O$ (1–0), ^{12}CO (3–2), ^{12}CO (4–3), [C I] $^3P_1$–$^3P_0$, $H^{12}CO^+$ (4–3), $H^{13}CO^+$ (4–3), and 870 μm continuum emission. These data suggest that the source for the FIR line and continuum emission, and the driving source for the molecular outflow, is a yet-unidentified Class 0 source deeply embedded in the cloud. Using HCO^+ and continuum observations, we derive a core gas mass of about 0.5 $M_\odot$. From a centroid velocity analysis of the HCO^+ emission, we estimate the mass enclosed inside the rotating molecular disk to be $\sim$0.75 $M_\odot$. Both these measurements suggest the presence of a low-mass (0.5 $M_\odot$) protostar surrounded by an envelope of similar mass.

Line shapes show evidence of infall, rotation, and outflow motions in the central $60'' \times 60''$ of the map. The outflow dominates the line formation outside this region. The outflow mass is at least 0.84 $M_\odot$, similar to the mass of the protostar that we believe is driving the outflow. The energetics are typical for a molecular outflow around a young, low-mass protostar, with a mechanical luminosity much less than the FIR luminosity.

Our result supports the ''standard'' model for low-mass star formation. Follow-up with millimeter-wave interferometers in both continuum and high-density molecular tracers could reveal the Class 0 source, if present, and allow detailed study of the infall and rotational motions of the molecular disk.

We thank the staff of the Arizona Radio Observatory, particularly Harold Butner, for collecting the 870 μm continuum data during priority observing mode. We also thank the staff of the Antarctic Submillimeter Telescope and Remote Observatory for their support of the AST/RO telescope. Michael Meyer, John Bieging, and Erick Young also participated in valuable discussions. This research was supported in part by the National Science Foundation, under a cooperative agreement with the Center for Astrophysical Research in Antarctica (CARA), grant number NSF OPP 89-20223. Author C. Groppi thanks the National Science Foundation (grant number 0138318) and the National Aeronautics and Space Administration (grant number S01-GSRP-023) for their support.

REFERENCES

Adelson, L. M., & Leung, C. M. 1982, BAAS, 14, 606
Anderson, I. M., Harju, J., & Haikala, L. K. 1997a, A&A, 326, 366
Anderson, I. M., Harju, J., Knee, L. B. G., & Haikala, L. K. 1997b, A&A, 321, 575
Brown, A. 1987, ApJ, 322, L31
Chini, R., et al. 2003, A&A, 409, 235
Choi, M., & Tatematsu, K. 2004, ApJ, 600, L55
Draine, B. T., & Lee, H. M. 1984, ApJ, 285, 89
Harju, J., Haikala, L. K., Mattila, K., Mauersberger, R., Booth, R. S., & Nordh, H. L. 1993, A&A, 278, 569
Henning, Th., Launhardt, R., Steinacker, J., & Thamm, E. 1994, A&A, 291, 546
Hildebrand, R. H. 1983, QJRAS, 24, 267
Hogerheijde, M. R. 2002, in SFChem 2002: Chemistry as a Diagnostic of Star Formation, ed. C. L. Curry & M. Fich (Ottawa: NRC Press), 44
Levreault, R. M. 1988, ApJS, 67, 283
Loren, R. B. 1979, ApJ, 227, 832
Marraco, H. G., & Rydgren, A. E. 1981, AJ, 86, 62
Narayanan, G., Walker, C. K., & Buckley, H. D. 1998, ApJ, 496, 292 (erratum 530, 1105 [2000])
Shu, F. H. 1977, ApJ, 214, 488
Snell, R. L., Scoville, N. Z., Sanders, D. B., & Erickson, N. R. 1984, ApJ, 284, 176
Stahler, S. W., Shu, F. H., & Taam, R. E. 1980, ApJ, 242, 226
Stark, A. A., et al. 2001, PASP, 113, 567
Stutzki, J., Stacey, G. J., Genzel, R., Harris, A. I., Jaffe, D. T., & Lugten, J. B. 1988, ApJ, 332, 379
Taylor, K. N. R., & Storey, J. W. V. 1984, MNRAS, 209, 5P
Walker, C. K., Adams, F. C., & Lada, C. J. 1990a, ApJ, 349, 515
Walker, C. K., Carlstrom, J. E., Bieging, J. H., Lada, C. J., & Young, E. T. 1990b, ApJ, 364, 173
Walker, C. K., Lada, C. J., Young, E. T., Maloney, P. R., & Wilking, B. A. 1986, ApJ, 309, L47
Walker, C. K., Narayanan, G., & Boss, A. P. 1994, ApJ, 431, 767
Walker, C. K., Narayanan, G., Büttgenbach, T. H., Carlstrom, J. E., Keene, J., & Phillips, T. G. 1993, ApJ, 415, 672
Wilking, B. A., Harvey, P. M., Joy, M., Hyland, A. R., & Jones, T. J. 1985, ApJ, 293, 165
Wilking, B. A., McCaughrean, M. J., Burton, M. G., Giblin, T., Rayner, J. T., & Zinnecker, H. 1997, AJ, 114, 2029